International Journal of Mining and Geo-Engineering

IJMGE

IJMGE 53-2 (2019) 143-150

DOI: 10.22059/ijmge.2019.272707.594774

One-Dimensional Modeling of Helicopter-Borne Electromagnetic Data Using Marquardt-Levenberg Including Backtracking-Armijo Line Search Strategy

Fereydoun Sharifi [a], Alireza Arab-Amiri [a, *], Abolghasem Kamkar-Rouhani [a], Ralph-Uwe Börner [b]

[a] *Faculty of Mining, Petroleum and Geophysics, Shahrood University of Technology, Shahrood, Iran*

[b] *Institute of Geophysics and Geoinformatics, TU Bergakademie Freiberg, Freiberg, Germany*

Article History:

Received: 30 December 2018,

Revised: 15 April 2019

Accepted: 22 April 2019.

ABSTRACT

In the last decades, the helicopter-borne electromagnetic (HEM) method has become a focus of interest in mineral exploration, geological mapping, groundwater resource investigation, and environmental monitoring. As a standard approach, researchers use 1D inversion of the acquired HEM data to recover the conductivity/resistivity-depth models. The relationship between HEM data and model parameters is strongly nonlinear. In the case of dealing with simple 1D models, in which the number of model parameters is less than the number of measured data, i.e., an overdetermined system, the conventional approach to recover the model parameters is to implement regularized nonlinear least square methods. Among the least square methods, Marquardt-Levenberg acts as an integrated optimization algorithm that comprises both the gradient-descent and Gauss-Newton strategies. This algorithm resolves the deficiencies of slow convergence of gradient-descent and the singularity of the sparse matrix in the Gauss-Newton algorithm. Also, the line search strategy improves the objective function to ensure that the algorithm converges to the optimum global point. In this study, the Marquardt-Levenberg algorithm, including the backtracking-Armijo line search, was implemented for HEM data inverse modeling. Moreover, a linear filter of the Fast Hankel Transform (FHT) was used to find the forward operator for data simulation.

Developing the proposed algorithm through programming with MATLAB, a resistivity model of underlying layers was obtained successfully. The algorithm was employed to recover a resistivity model from the HEM data acquired above the Alut region located in the northwest of Iran, which is a shear zone structure consisting of chlorite schist, phyllite/phyllonite, metamorphosed limestone/dolomite, mylonite, and ultra-mylonite units. As a result, according to the geological map of the study area, a resistivity-depth section of subsurface layers was successfully derived along the HEM flight line. The results detected a plausible shear zone and a mylonitic granite as favorable targets for the orogenic gold mineralization.

Keywords : *HEM, Inverse Modeling, Marquardt-Levenberg, Backtracking-Armijo Line Search, Orogenic Gold Mineralization*

1. Introduction

Helicopter-Borne Electromagnetic (HEM) systems are suitable for high resolution, fast, and relatively cost-effective surveys for mapping the electrical resistivity/conductivity distribution of a large-scale area [1, 2]. These systems are equipped with a towed rigid-boom EM system hanging 30-40 m below the helicopter [1]. The two standard HEM systems, DIGHEM and RESOLVE, are frequency-domain multi-coil systems consisting of five and six small transmitters (T_x) and receiver (R_x) coils, respectively (Fig. 1).

The coil configuration is set up based on the orientation of the transmitter and receiver coils. The transmitter is oriented in a horizontal or vertical position, and the receiver coil is configured in the horizontal coplanar (HCP), vertical coplanar (VCP), or vertical coaxial coil (VCX) systems depending on maximum couple between T_x and R_x [1]. In order to conduct the HEM survey, the transmitter excites a harmonic oscillating primary magnetic field inducing eddy currents within the underground conductive bodies. [1, 3]. The eddy currents, in turn, generate a secondary magnetic field that is added to the source field in the entire magnetic field recorder using a receiver coil installed on the EM system. Next, the source field is subtracted from the measured total magnetic field to recover the secondary magnetic field that is later normalized by the source field. The normalized secondary magnetic field is usually presented in parts per million (ppm) [1, 3]. Then, the secondary magnetic behavior is interpreted to reveal the characteristics of conductive mass [3, 4].

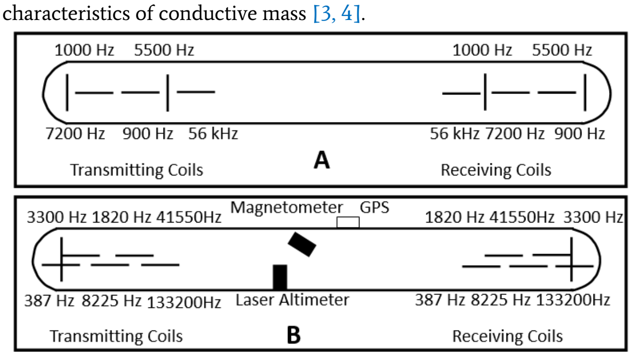

Fig. 1. Coil configuration in DIGHEM (A) and RESOLVE (B) frequency-domain EM systems [after 1, 2].

* Corresponding author. Tel. +98-2332392204, *E-mail address:* alirezaarabamiri@yahoo.com (A. Arab-Amiri).

Various 1D [1, 2, 5-9], 2D [10-13], and 3D [14-17] forward and inverse modeling methods of well-known Maxwell's equations provide meaningful interpretations of acquired HEM data.

As the main advantages of 1D modeling, it may serve the analytical solution with significant computational efficiency superiority while 2D and 3D modeling approaches are numerical solutions only. Therefore, the 1D data inversion is still an interesting topic for the researchers (e.g., [18]). The use of inverse Laplace transform is a common approach to implement Maxwell's equation in the 1D forward modeling. [1, 19]. The obtained integral relation is called Hankel integral, which cannot be solved analytically, and hence, numerical methods are used to solve it [1]. Here, a general approach for the calculation of 1D Hankel integrals is to use Fast Hankel Transform (FHT) with linear filters to discretize the Hankel integral (e.g., [20-22]).

Recovering the model parameters, e.g., the thicknesses and electrical conductivities/resistivities of layers, from electromagnetic data demands to employ an inversion algorithm. Among data inversion techniques, Occam's inversion [23- 25], Gauss-Newton [26], and Levenberg-Marquardt (LM) [27] are popular algorithms for 1D nonlinear inversion of HEM data.

In this paper, the FHT was used for forward calculations. Also, the LM method, including the backtracking-Armijo line search, was used for 1D data inversion to recover the model parameters, i.e., the resistivities and the thicknesses of layered areas, from both the synthetic and field HEM data recorded above the Alut area in northwest Iran.

2. Modeling

2.1. Forward modeling

Generally, a forward operator is required to simulate the HEM data. Accordingly, this study follows some pioneering research works [2, 19, 28-30]. Assuming the coil separation r and the sensor altitude h, the relative secondary magnetic field Z and X of a horizontal coplanar and vertical coaxial coil pair are given by

$$Z = r^3 \int_0^\infty R_{TE}(f, \lambda, \rho, \mu, \varepsilon) \frac{\lambda^3 e^{-2h\alpha_0}}{\alpha_0} J_0(\lambda r) d\lambda \tag{1}$$

And

$$X = r^2 \int_0^\infty R_{TE}(f, \lambda, \rho, \mu, \varepsilon) \lambda e^{-2\lambda h} \frac{J_1(\lambda r) - \lambda J_0(\lambda r)}{2} d\lambda , \tag{2}$$

respectively.

Here,

$$\alpha_0^2 = (\lambda^2 - \omega^2 \mu_0 \varepsilon_0 + i\,\omega\mu_0 / \rho_0) \tag{3}$$

Where μ_0 denotes magnetic permeability, ε_0 is dielectric permittivity, ρ_0 is the resistivity of free space, J_0 and J_1 are the Bessel function of the first kind and zero and first order respectively, R_{TE} is complex reflection coefficient, and λ is wave number.

A recurrence relation gives the complex reflection coefficient RTE for an n-layer half-space, as:

$$R_{TE} = \frac{\beta_1 - \alpha_0 . \mu / \mu_0}{\beta_1 + \alpha_0 . \mu / \mu_0} \tag{4}$$

where

$$\beta_k = \alpha_k((\beta_{k+1} + \alpha_k . \tanh(\alpha_k t_k)) / (\alpha_k + \beta_{k+1} . \tanh(\alpha_k t_k))), \quad k = 1, 2, ..., n \tag{5}$$

$$\alpha_k^2 = (\lambda^2 - \omega^2 \varepsilon_k \mu_k + i\,\omega\mu_k / \rho_k), \quad k = 1, 2, ..., n \tag{6}$$

β_n is surface admittance, and α_n is characteristic admittance, ρ_n, μ_n, ε_n and t_n denote resistivity, magnetic permeability, dielectric permittivity and thickness of layers, respectively. The magnetic permeability and dielectric permittivity are set to their free space values in this paper ($\mu_0 = 4\pi \times 10^{-7}$, $\varepsilon_0 = 8.8542 \times 10^{-12}$). The last layer of the model is a half-space and thus, as the thickness of half-space goes infinity, and hyperbolic tangent value of infinity equals 1, considering the equation (5), $\beta_n = \alpha_n$.

To numerically compute the Hankel integral in equation (1), we used the Guptasarma, and Singh's [22] approach with a 61-point and 120-point filter for the Hankel J_0 transform and 47-point and 140-point filter for the Hankel J_1 transform. Therefore, the Hankel integral was transformed in the equation (1) using,

$$Z = r^2 \sum_{i=1}^{n} (R_1 \frac{\lambda_i^3 . \exp(-2h . \alpha_0)}{\alpha_0}) W_i \tag{7}$$

The secondary magnetic field of vertical coaxial coil pair can be approximated as follow,

$$X \approx -\frac{Z}{4} \tag{8}$$

$$\lambda_i = (\frac{h}{r}) \times 10^{((i-1)s + a)} \tag{9}$$

where W_i is the 120-point J_0 and 140-point J_1 filter weights, a and s are some constant values which in the case of 120-point J_0 filter $a = -8.3885$ and $s = 9.04226468670\text{e} \times 10^{-2}$ and in the case of 140-point J_1 filter $a = -7.91001919000$ and $s = 8.79671439570 \times 10^{-2}$ [22].

2.2. Inverse modeling

The functional relationship between the model parameter and the observed HEM data given in relation (4) could be rewritten in operator notation as

$$d = f(m), \tag{10}$$

where d denotes observed data which could be assembled into data vector as $\boldsymbol{d} = [d_1, d_2, ..., d_i]^T$, f is nonlinear forward operator and $\boldsymbol{m}$ is the unknown model parameters that could be assembled into model vector $= [\rho_1, \rho_2, \rho_3, \rho_4, t_1, t_2, t_3]^T$ where superscript T denotes transpose.

Typically, the number of model parameters (j) exceeds the number of measured HEM data (i) that constrain them, and therefore, this problem represents the underdetermined inverse problem that demands robust iterative model space solution algorithm that takes regularization into account in order to achieve a stable solution. Regularized non-linear least-square based algorithms are modified in order to satisfy these criterions [31].

In this approach, the inversion is implemented using the Tikhonov regularization scheme [31, 32] by minimizing the data misfit subject to a constraint on the model parameters

$$\varphi(\boldsymbol{m}) = \|\boldsymbol{d} - f(\boldsymbol{m})\|^2 + \eta \|W_m \boldsymbol{m}\|^2 \tag{11}$$

where η is a regularization parameter, and W_m is the weighting matrix of the model.

In order to speed up the convergence [32], the algorithm updates the regularization parameter using a geometric progression,

$$\eta_k = \eta_1 q^{k-1} \tag{12}$$

where η_1 is an initial value and can be found after a finite number of trials, $0 < q < 1$, and k is the iteration number.

A well-known Marquardt-Levenberg algorithm was developed to stabilize the inversion and overcome the ill-condition or singularity problem, which mainly arises from a large number of model parameter [31]. Here, 1D inversion of HEM data was implemented using this algorithm to recover the model parameters.

2.2.1 Marquardt-Levenberg Algorithm and Line Search Strategy

Marquardt-Levenberg is a standard algorithm that involves regularization for avoiding the singularity problem of the non-linear least-square optimization method. In this method, minimizing the cost function $\varphi(m)$ (equation (11)) for a nonlinear function f(m) gives equation (13)

$$(J^T J + \eta Wm) \delta m = J^T . r \tag{13}$$

Where J is the Jacobian matrix (size i by j), δm is the search direction, r is the difference between the observed data and the model response.

The weighting matrix of the model was considered as the identity matrix ($W_m = I$), but it could also be a finite difference approximation of the first or second derivative for higher-order regularization [25, 31].

The model parameter is updated using the relation

$$m_{k+1} = m_k + l . \delta \boldsymbol{m} \tag{14}$$

where l is the step length.

In practice, the algorithm starts at the initial model (m_0) and generates a sequence of iterations that stop when an appropriate termination criterion is satisfied, including either that the problem has been solved within the desired accuracy, or that no further progress can be made.

Calculating the model update in each iteration demands a reliable approach for the modification of the initial model in which both a search direction and a step length of the move toward the next iteration could be found efficiently. In this study, the line search strategy was used based on the Armijo condition [33]. This method is reiterated so that the step length l provides sufficient decrease in the objective function φ, i.e., the step length is acceptable only if the following inequality is satisfied

$$\varphi(m_{k+1}) \le \varphi(m_k) + c.l.J(m_k)^T.\delta \boldsymbol{m} \tag{15}$$

Where $c \in (0,1)$ is a constant value. Hence, the decline of φ is proportional to both the step length and the directional derivative $J(m_k)^T.\delta \boldsymbol{m}$.

Equation 15 is a backtracking line search process using the Armijo condition. The line search starts by setting the direction search to $\delta \boldsymbol{m}$ and then determines an appropriate step length using a trial and error procedure. After a finite number of trials, starting from 1 as the initial value, the step length changed to reach an acceptable value. Then, l is eventually become sufficiently small to reach a threshold limit [33].

The following algorithm shows how the cost function value in iteration k is update to get a sufficient decrease and move to iteration $k+1$ [33],

Backtracking line search based on Armijo condition

Choose $s.l=1$, $c=10^{-4}$; **set** $l \leftarrow s.l$;

Repeat until $\varphi(m_{k+1}) \le \varphi(m_k) + c.l.J(m_k)^T.\delta m$

$l \leftarrow 0.25l$

End

2.2.2. Defining the Jacobian Matrix

To avoid the scale effect and to force the constraint to lie in a positive value, the model parameter was transformed using log-transformation, and then, obtained the Jacobian matrix by taking an exact partial derivative of the forward operator concerning the model parameter [9]. The elements of the Jacobian matrix is given by

$$J_{ij} = \frac{\partial Z_i}{\partial \log 10(m_j)} \tag{16}$$

Matrix J shows the sensitivity of the ith model response due to a change in the jth model parameter.

In order to evaluate the reliability of the computed Jacobian, the derivative test was used using Taylor expansion [14, 34]. Fig. 2 displays the result of Taylor expansion test for a computed Jacobian matrix in this study. The solid red and blue lines represent the first and second order approximation of Taylor series, respectively, and the solid red circle shows the precision of approximation for arbitrary random $\boldsymbol{m}$ vector versus $\boldsymbol{h} \in \left[10^{-10}, 10^{-1}\right]$. The error of second-order approximation, $e_2(h)$, is calculated as follows:

$$e_2(\boldsymbol{h}) = \left\| f(\boldsymbol{m} + \boldsymbol{h}.\Delta m) - f(\boldsymbol{m}) - \boldsymbol{h}.J(\boldsymbol{m}).\Delta m \right\|_2^2 \tag{17}$$

As it could be found in Fig. 2, the calculated Jacobian matrix satisfies the Taylor expansion test and converges to the second-order of approximation, perfectly.

3. Results and discussion

3.1. Synthetic model

A forward and inverse modeling code was developed to recover the resistivity and the thickness of a layered half-space model from 1D HEM data using MATLAB. Also, a 4-layer model (Fig. 3) was constructed based on model parameters similar to the case mentioned by Siemon et al. [8]. Then, a survey was conducted using a frequency-domain multi-coil system RESOLVE with four horizontal coplanar coils and one vertical coaxial coil with a coil separation of 8 m and a sensor at the height of 30 m above the surface suspended from a helicopter. Same as the RESOLVE operating system, the frequencies used in this study were 0.9, 1, 5.5 and 7 KHz for coil separation of 7.86 m, and a 56 KHz frequency for coil separation of 6.3m [1, 2].

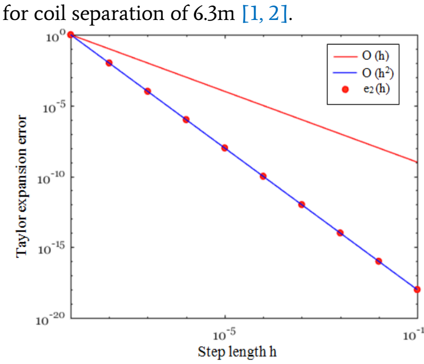

Fig. 2. The result of the Taylor expansion test for validation of the Jacobian matrix. The axes are both scaled logarithmically.

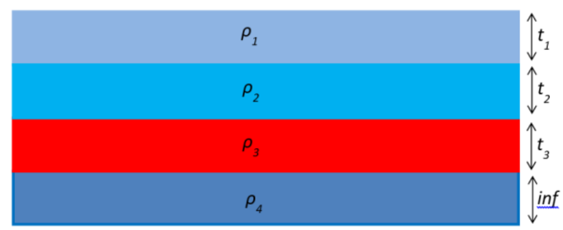

Fig. 3. A Sketch of a synthetic 4-layered model. The model parameters consist of resistivity (ρ) and thickness of layers (t).

In the first step, two different sets of data were generated from the synthetic model denoted by sounding A and sounding B using the model parameters given in Table 1 [8].

Table 1. Model parameters of a 4-layered ground [8].

Model parameters	ρ_1	ρ_2	ρ_3	ρ_4	t_1	t_2	t_3
Sounding A	50	100	5	1000	20	30	10
Sounding B	200	100	5	1000	20	30	10

The obtained data is tabulated in Table 2. This verifies that the performance of the forward model response in this study is similar to that of Siemon et al. 's (Table 3) [8]. Fig. 4 and Table 2 display the real and imaginary part and phase of the obtained synthetic data for Soundings A and B. These figures show that while the calculated phase of sounding A is slightly larger than that of sounding B in the low frequencies. In high frequencies, the phase shift of sounding B increases compared to sounding A. This characteristic appears concerning the resistivity of the upper layer. Therefore, the depth of investigation in EM methods depends on both frequency and resistivity. In higher frequencies, as the resistivity of the upper layer of sounding A is less than that of sounding B, a skin depth of sounding A is less than that of sounding B. Considering equations (6) and (7), the smaller the resistivity of upper layer, the larger the obtained imaginary part of HEM response, and therefore, the obtained phase increases.

Table 2. Acquired HEM data for soundings A and B above the 4-layer synthetic model depicted in Fig. 3 with the model parameters given in Table 1.

HEM	Sounding A			Sounding B		
f (Hz)	R (ppm)	Q (ppm)	Phase (milli-radian)	R (ppm)	Q (ppm)	Phase (milli-radian)
387	27.471	103.99	1312.5	21.8452	68.8533	1263.6
1820	168.51	295.22	1052.1	129.62	166.29	908.68
8225	514.19	700	937.25	282.49	297.4	811.11
41550	1705	1199.9	613.23	744.45	769.25	801.78
133200	2742.2	1128.6	390.44	1535.4	1085.6	615.42

***R is the real part (in-phase), and Q is the imaginary part (Quadrature) of acquired complex data.**

Table 3. Obtained HEM data for soundings A and B above the 4-layer synthetic model depicted in Fig. 3 using FHT method developed by Federal Institute for Geosciences and Natural Resources of Germany (BGR) and HydroGeophysics Group (HGG) of the University of Aarhus, Denmark [8].

HEM	Sounding A				Sounding B			
	BGR (FHT)		HGG (FHT)		BGR (FHT)		HGG (FHT)	
f (Hz)	R (ppm)	Q (ppm)	R (ppm)	Q (ppm)	R (ppm)	Q (ppm)	Q (ppm)	R (ppm)
387	27.41	102.8	27.42	103	21.8	68.36	21.8	68.44
1820	167.7	290.3	167.8	291.1	129.1	164.4	129.2	164.7
8225	508.7	682.2	509.6	685.2	280.4	291.5	280.8	292.4
41550	1667	1149	1673	1158	734.7	747.4	736.4	750.8
133200	2655	1069	2671	1079	1506	1047	1512	1053

Next, to evaluate the effect of varying the resistivity of the upper layer and the buried conductive layer, four scenarios were considered (Table 4) to simulate the responses of the horizontal coplanar-coil configuration of DIGHEM system in the frequency range of 900 Hz to 56 KHz via equation (7). Figs 5 and 6 show the real and the imaginary parts and the phase of the synthetic data for all four scenarios. In the first and second scenarios, the resistivity of the upper layer is the same (50 ohm·m) but the resistivity of the third layer of the first scenario varies from 10 to 100 with intervals of 10 ohm.m, and it varies from 1 to 10 with intervals of 1 ohm.m in the second one. Fig. 5 shows a comparison between the models' responses for the first and second scenarios and reveals that in the first scenario, the phase magnitude is stronger than the second scenario. Moreover, the varying of the phase shift with frequency is sharper in the first scenario. It happens due to the concentration of eddy currents in conductive layers, which decreases the calculated resistivity and consequently decreases the phase. The larger the conductivity of the third layer, the smaller the phase.

Table 4. Model parameters of 4-layered earth (resistivity of the upper layer and anomalous layer are varying). The resistivity of the third layer, ρ_3 in the 2nd and 4th scenarios is varying in the range of 10 to 100 ohm.m with 10 ohm.m intervals.

Model parameters	ρ_1	ρ_2	ρ_3	ρ_4	t_1	t_2	t_3
Scenario 1	50	100	10-100	1000	20	30	10
Scenario 2	50	100	1-10	1000	20	30	10
Scenario 3	500	100	10-100	1000	20	30	10
Scenario 4	500	100	1-10	1000	20	30	10

In order to validate the inversion code, the resistivity and thickness of the synthetic model were recovered from 1D inversion of HEM data of sounding A and B (Table 2). Table 5 shows the result of inversion for noise-free and noisy data with 5% and 10% of white-noise data. The inversion code ideally recovered the model parameters from noise-free data. However, the inversion of noisy data gives the model parameters with the RMS errors (Fig. 7) given in Table 6. This Table also represents the elapsed time (ET) and several iterations (NOI) of the algorithm to converge to the optimum point for both Soundings A and B. As the table shows, the algorithm is quite fast and recovers the optimum model parameters in a few iterations with a small elapsed time.

Table 5. Recovered model parameters from HEM data for soundings A and B using the Marquardt-Levenberg algorithm. Resistivity (ρ) and thickness (t) values are in ohm.m and meter, respectively.

HEM sounding	*Sounding A*			*Sounding B*		
Model parameters	*Free noise*	*5% noise*	*10% noise*	*Free noise*	*5% noise*	*10% noise*
ρ_1	*50*	*52.92*	*56.16*	*200*	*223.89*	*253.98*
ρ_2	*100*	*105.60*	*107.75*	*100*	*101.15*	*99.78*
ρ_3	*5*	*2.87*	*2.42*	*5*	*2.91*	*2.94*
ρ_4	*1000*	*900.54*	*899.80*	*1000*	*902.28*	*901.80*
t_1	*20*	*23.63*	*31.29*	*20*	*16. 59*	*15.00*
t_2	*30*	*33.73*	*42.05*	*30*	*37.99*	*42.46*
t_3	*10*	*5.87*	*6.72*	*10*	*5.76*	*5.63*

Table 6. RMS, elapsed time (ET) and number of iteration (NOI) of inversion to recover the model parameters.

HEM sounding	*Sounding A*			*Sounding B*		
	Free noise	*5% noise*	*10% noise*	*Free noise*	*5% noise*	*10% noise*
ET (seconds)	*0.365405*	*0.241528*	*0.240953*	*0.32*	*0.31*	*0.29*
RMS (%)	*0.0836*	*6.8191*	*15.86*	*0.47*	*5.95*	*12.1*
NOI	*8*	*5*	*5*	*6*	*5*	*5*

Fig. 6 displays the third and fourth scenarios. In these scenarios, the phase also decreases by decreasing the resistivity of the third layer from 100 to 1 ohm.m. The comparison between Figs 5 and 6 indicates that the larger the resistivity of the upper layers, the smaller the magnitude of phase. In scenarios 3 and 4, the depth of penetration of eddy currents is deeper than scenarios 1 and 2. Therefore, the density of eddy currents in the third layer of scenarios 3 and 4 increases, and it causes the phase to become smaller than their counterparts in scenarios 1 and 2.

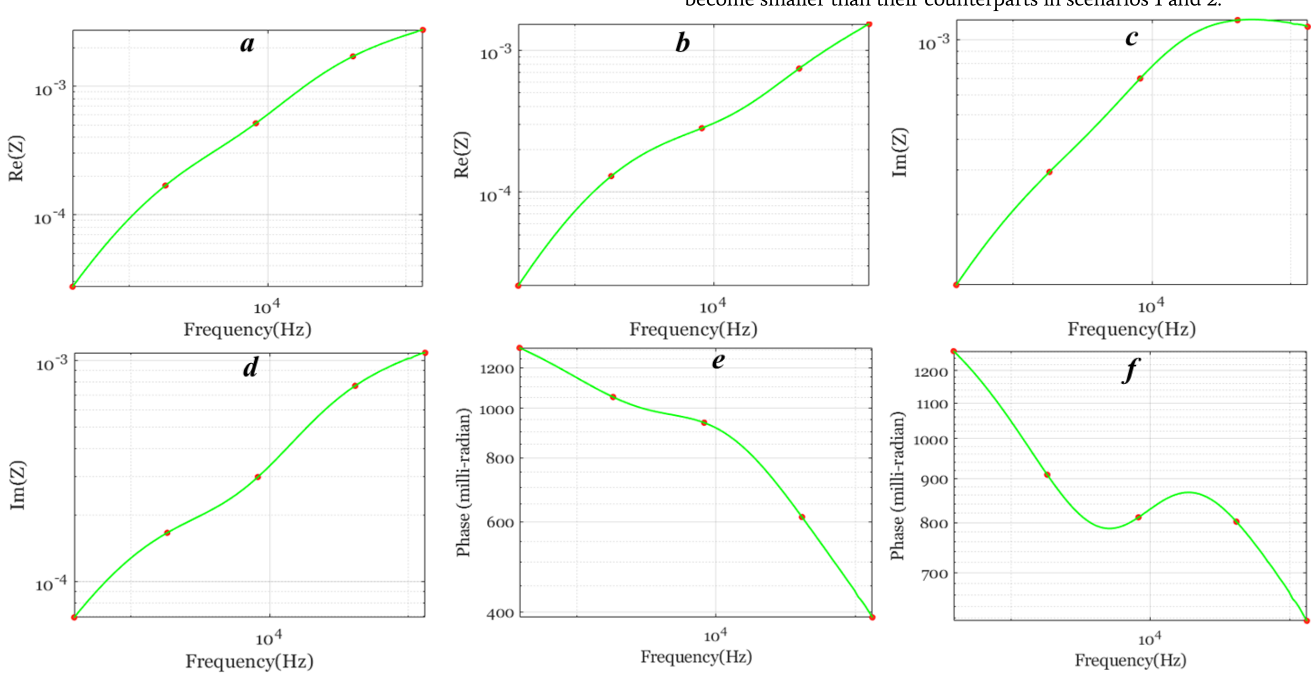

Fig. 4. Real part (a & b), imaginary part (c & d) and phase (e & f) of the secondary magnetic field of HEM normalized to the primary magnetic field for soundings A (left side column) and B (right side column) respectively. The results are based on the HEM data given in Table 2.

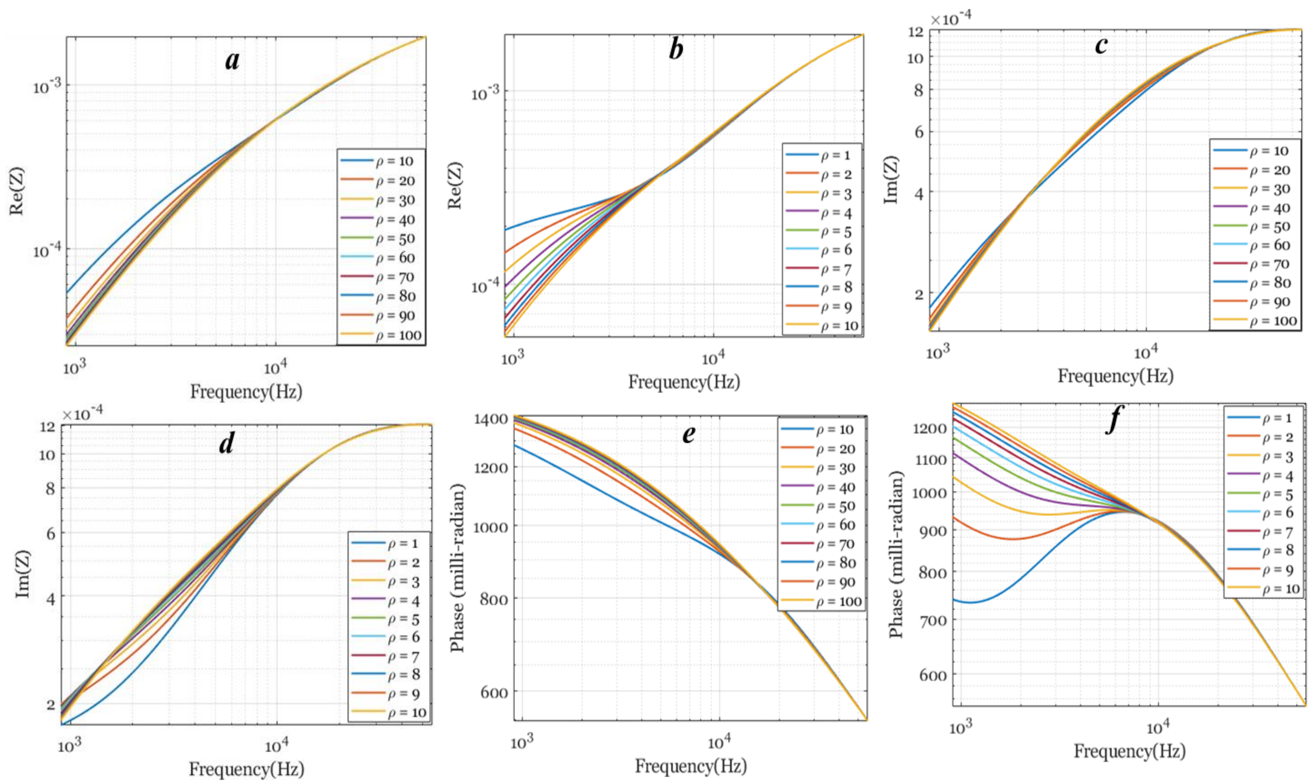

Fig. 5. Real part (a & b), Imaginary part (c & d) and phase (e & f) of scenario 1 (left side column) and scenario 2 (right side column) given in Table 4.

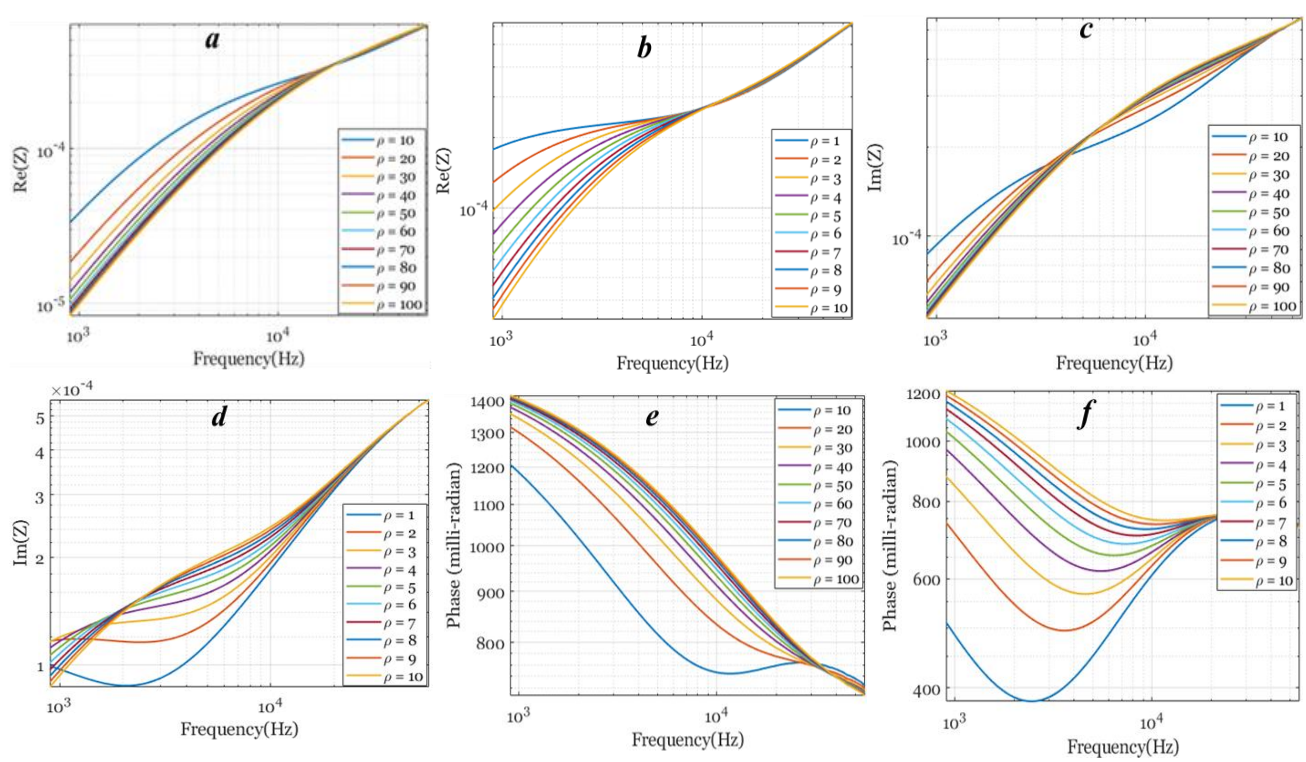

Fig. 6. Real part (a & b), Imaginary part (c & d) and phase (e & f) of scenario 3 (left side column) and scenario 4 (right side column) given in Table 4.

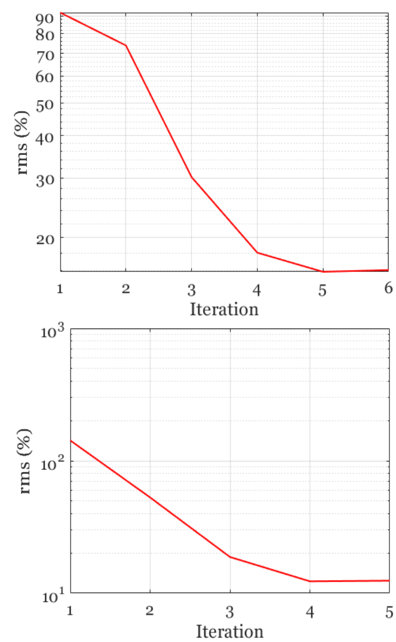

Fig. 7. RMS data misfit versus iteration number for inversion of sounding A (left panel) and sounding B (right panel) using Levenberg-Marquardt algorithm.

[Fig. 8](#) shows the real and the imaginary parts and phase of the noisy synthetic data, and predicts the data as the response of final estimated model for both soundings A and B. The predicted data almost fits the synthetically produced noisy data.

3.2. Study area

The Study area is located in the Alut region, at the northern part of Sanandaj-Sirjan metamorphic zone (SSZ), northwest of Iran. A regional ductile-brittle deformation shear zone exists in the area. The rock formation in the study area consists of Mesozoic volcanic-sedimentary sequences, with mafic to mostly acidic meta-volcanic rocks. Geological studies confirmed the presence of sericite schist, chlorite schist, Phyllite, Phyllonite (in the sheared parts), interbedded limestone and dolomite, quartzite in the area. Altered shear zones include mylonite and ultra-mylonite, and metamorphosed felsic to mafic rocks [35- 37]. Fig. 9 displays the geological map of the study area.

Fig. 9 shows that the direction of HEM survey profile is almost perpendicular to the strike of geological units. In this study, the acquired DIGHEM data was integrated along the profile line using HCP and VCX coil configuration to recover the model parameter from the HEM data acquired by FUGRO airborne surveys corporation above the Alut region in 2004.

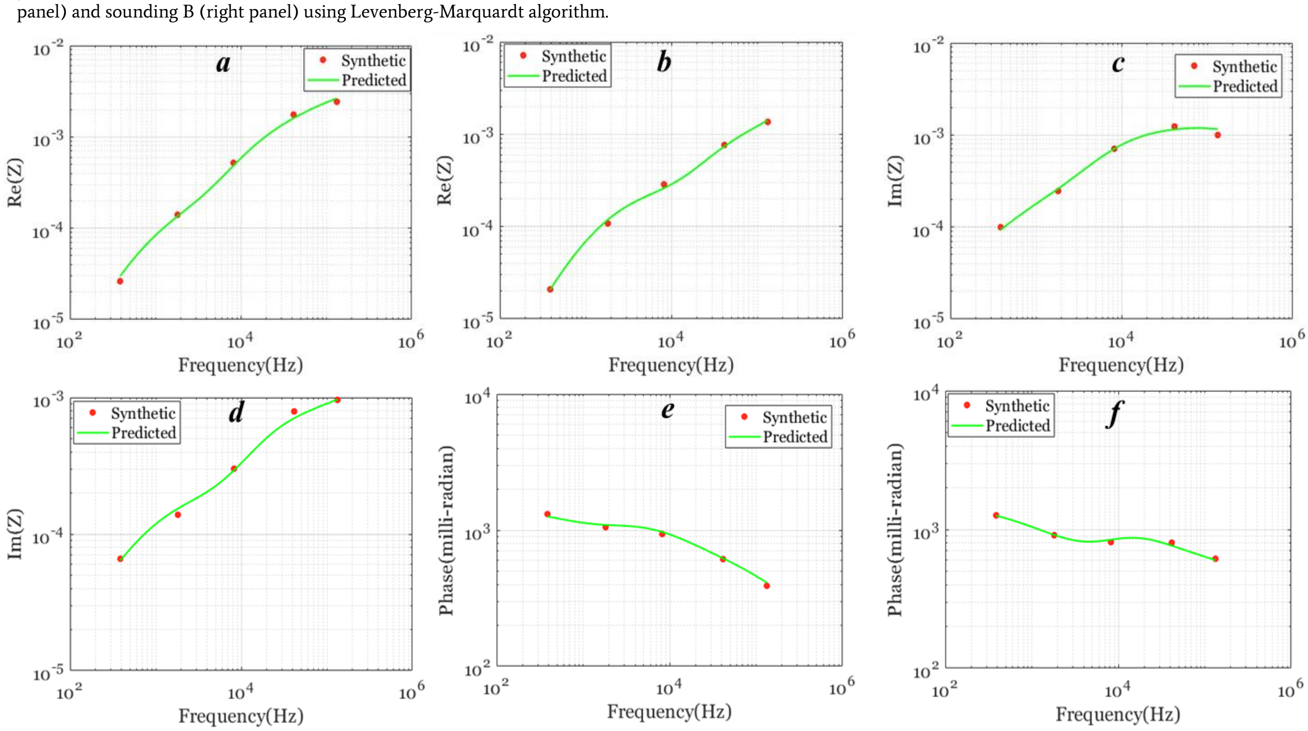

Fig. 8. A comparison between real part (a & b), imaginary part (c & d) and phase shift (e & f) of the synthetic data and the predicted data as a response of the final estimated model. The results are shown for sounding A (left side column) and B (right side column). The synthetic data, associated with 10% noise, is depicted by the solid red points.

In this 1D data inversion algorithm, a 5-layer ground was defined using equation (12) with the regularization factor η_1=1.05×10^{-08} and q = 0.7. Then, equation (17) was used to calculate the mean resistivity of each layer as the geometric mean of the recovered resistivities from HCP and VCX.

Next, the average resistivities and the thicknesses of layers were used stitched together to display the resulting resistivity model from 1D sounding. Same as the geological map of the study area (Fig. 9), Fig. 10 depicts a moderate range of resistivity for metamorphosed limestone and dolomite (between 2000-4000 ohm.m), relatively lower resistivity (between 1000-2000 ohm.m) corresponding to the mineralized shear zone (the pink regions in the map shown in Fig. 9), the lower resistivity values (<1000 ohm.m) due to presence of phyllite and other foliated metamorphic rocks. It is expected that the high values of resistivities (> 4000 ohm.m) may be related to the mylonitic granite unit rock in the area. Also, the conductive unit outlined with ACU on the map was attributed to either a buried phyllite unit or altered rock unit close to the desired mylonitic granite unit that could be considered as a plausible indicative of orogenic gold mineralization. Therefore, based on these explanations, there was an excellent agreement between the geophysical patterns and the geologic units identified on the map.

Detailed exploration should be followed using ground-based geophysical methods including resistivity (Res.) induced polarization (IP) surveys to delineate plausible resistive silicified alteration and polarizable sulfidic alterations that are often associated with the type of gold deposit being explored. Moreover, conducting the litho-geochemical surveys on the detected plausible auriferous rock units might reduce the uncertainties associated with geophysical methods and provide more reliable information to assess the gold mineralization occurrence and targeting mineral exploration drilling in the area.

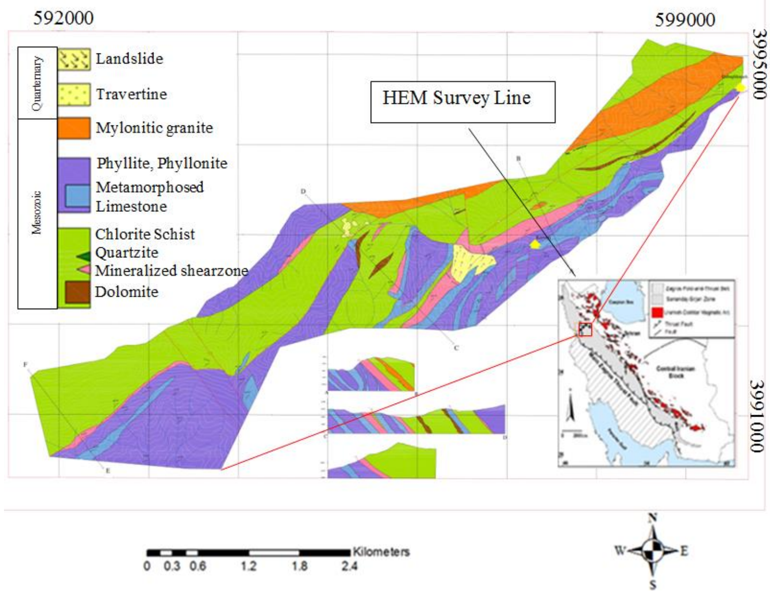

Fig. 9. Geological map of the study area. The black color solid line depicts the HEM flight line (after [40]).

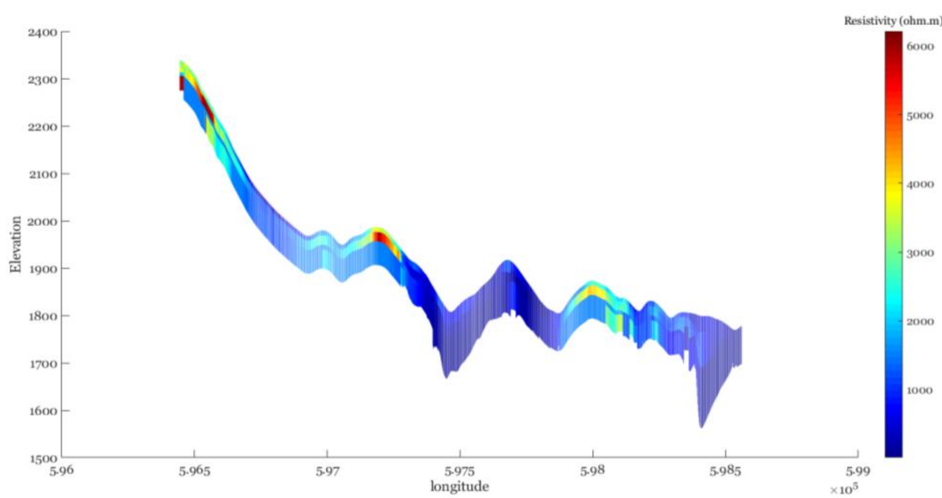

Fig. 10. 1D map of stitched average resistivities and thicknesses of layers together along the profile line shown in Fig. 9.

4. Conclusions

This paper implemented the FHT and Marquardt-Levenberg algorithm to retrieve a resistivity-depth model from the HEM data acquired from the Alut area where a high geological potential of orogenic gold occurrence exists. The recovered resistivity model using the proposed approach is in agreement with the geological map of the study area. Both types of desired rock formations for the orogenic gold occurrence, including resistive mylonitic granite and the mineralized shear zone, can be successfully detected on the resistivity section. However, the lateral parameters were not taken into account for 1D modeling of the HEM data. Including these parameters may increase the accuracy of modeling, and thus, provide a more reliable resistivity model. For the next exploration plan, conducting more exploratory surveys such as ground-based geophysical IP-Res methods is recommended on favorite rock formations. This process helps geologists to investigate the auriferous quartz veins and sulfidic minerals such as pyrite that may be formed in the silicified and polarizable sulfidic alteration zones associated with the type of gold deposit being explored.

Acknowledgments

F. Sharifi gratefully thanks Prof. Klaus Spitzer for his complete support, and also, Dr. Mathias Scheunert and Dr. Jana Börner for their valuable pieces of advice. Also, the authors gratefully thank reviewers for their careful reading of our manuscript and their comments and questions that helped us to improve the manuscript.

REFERENCES

[1] Siemon, B., Christiansen, A.V. and Auken, E., (2009a). A review of helicopter-borne electromagnetic methods for groundwater exploration *Near Surface Geophysics*, 7(5-6), pp.629-646.

[2] Arab-Amiri, A.R., Moradzadeh, A., Fathianpour, N. and Siemon, B., (2011). Inverse modeling of HEM data using a new inversion algorithm. *Journal of Mining and Environment*. 1(2), 10-20.

[3] Scheunert, M. (2015). 3-D inversion of helicopter-borne electromagnetic data (Doctoral dissertation), *TU Bergakademie*

Freiberg, Germany.

[4] Dentith, M., & Mudge, S. T. (2014). Geophysics for the mineral exploration geoscientist. *Cambridge University Press*.

[5] Huang, H., & Fraser, D. C. (1996). The differential parameter method for multifrequency airborne resistivity mapping. *Geophysics*, *61*(1), 100-109.

[6] Farquharson, C. G., Oldenburg, D. W., & Routh, P. S. (2003). Simultaneous 1D inversion of loop–loop electromagnetic data for magnetic susceptibility and electrical conductivity. *Geophysics*, *68*(6), 1857-1869.

[7] Yin, C., & Hodges, G. (2007). Simulated annealing for airborne EM inversion. *Geophysics*, *72*(4), F189-F195.

[8] Siemon, B., Auken, E. and Christiansen, A.V., (2009b). Laterally constrained inversion of helicopter-borne frequency-domain electromagnetic data. *Journal of Applied Geophysics*, 67(3), pp.259-268.

[9] Siemon, B., (2012). Accurate 1D forward and inverse modeling of high-frequency helicopter-borne electromagnetic data. *Geophysics*, 77(4), WB71-WB87.

[10] Lavoué, F., Brossier, R., Métivier, L., Garambois, S., & Virieux, J. (2015). Frequency-domain modelling and inversion of electromagnetic data for 2D permittivity and conductivity imaging: An application to the Institut Fresnel experimental dataset. *Near Surface Geophysics*, *13*(3), 227-241.

[11] Mitsuhata, Y. (2000). 2-D electromagnetic modeling by finite-element method with a dipole source and topography. *Geophysics*, *65*(2), 465-475.

[12] Yu, W. W., & Haber, E. (2012). A 2.5 D inversion of airborne electromagnetic data. In *SEG Technical Program Expanded Abstracts 2012* (pp. 1-5). Society of Exploration Geophysicists.

[13] Wilson, G. A., Raiche, A. P., & Sugeng, F. (2006). 2.5 D inversion of airborne electromagnetic data. *Exploration Geophysics*, *37*(4), 363-371.

[14] Scheunert, M., Ullmann, A., Afanasjew, M., Börner, R. U., Siemon, B., & Spitzer, K. (2016). A cut-&-paste strategy for the 3-D inversion of helicopter-borne electromagnetic data—I. 3-D inversion using the explicit Jacobian and a tensor-based formulation. *Journal of Applied Geophysics*, *129*, 209-221.

[15] Cox, L. H., Wilson, G. A., & Zhdanov, M. S. (2010). 3D inversion of airborne electromagnetic data using a moving footprint. *Exploration Geophysics*, *41*(4), 250-259.

[16] Haber, E., Ascher, U. M., & Oldenburg, D. W. (2004). Inversion of 3D electromagnetic data in frequency and time domain using an inexact all-at-once approach. *Geophysics*, *69*(5), 1216-1228.

[17] Zhdanov, M., Alfouzan, F., Cox, L., Alotaibi, A., Alyousif, M., Sunwall, D., & Endo, M. (2018). Large-Scale 3D Modeling and Inversion of Multiphysics Airborne Geophysical Data: A Case Study from the Arabian Shield, Saudi Arabia. *Minerals*, *8*(7), 271.

[18] Kirkegaard, C.; Auken, E. (2015). A parallel, scalable and memory efficient inversion code for very large-scale airborne electromagnetics surveys. *Geophysical Prospecting*, 63, 495–507.

[19] Mundry, E. (1984). On the interpretation of airborne electromagnetic data for the two-layer case. *Geophysical Prospecting*, 32(2), 336-346.

[20] Johanson, H.K., Sørenson, K., 1979. Fast Hankel transforms. *Geophysical Prospecting* 27, 876–901.

[21] Anderson W.L. (1989). A hybrid fast Hankel transform algorithm for electromagnetic modelling. *Geophysics* 54, 263–266.

[22] Guptasarma, D., & Singh, B. (1997). New digital linear filters for Hankel J_0 and J_1 transforms. *Geophysical prospecting*, 45(5), 745-762.

[23] Constable, S. C., Parker, R. L., & Constable, C. G. (1987). Occam's inversion: A practical algorithm for generating smooth models from electromagnetic sounding data. *Geophysics*, *52*(3), 289-300.

[24] Shirzaditabar, F., & Oskooi, B. (2010). Recovering 1D conductivity from AEM data using Occam inversion. *Journal of Earth Space Physics*, *37*(3), 47-58.

[25] Aster, R. C., Borchers, B., & Thurber, C. H. (2011). Parameter estimation and inverse problems . *Academic Press*, 90, 169-192.

[26] Zhang, Z., Routh, P. S., Oldenburg, D.W., Alumbaugh, D. L., & Newman, G. A. (2000). Reconstruction of 1-D conductivity from dual-loop EM data. *Geophysics*, *65*(2), 492-501.

[27] Siemon B. (2006a). Electromagnetic methods – frequency domain: Airborne techniques. In: Groundwater Geophysics – A Tool for Hydrogeology (ed. R. Kirsch), pp. 155–170. Springer.

[28] Wait, J. R. (1982). Geo-electromagnetism,. *Academic*, San Diego, Calif, 268 pp.

[29] Siemon, B., Steuer, A., Ullmann, A., Vasterling, M., & Voß, W. (2011). Application of frequency-domain helicopter-borne electromagnetics for groundwater exploration in urban areas. *Physics and Chemistry of the Earth*, Parts A/B/C, 36(16), 1373-1385.

[30] Arab-Amiri, A.R., Moradzadeh, A., Rajabi, D., Siemon, B. & Fathianpour, N., (2010b). Deffinition and Comparison Improved Mundary's Integral with Mundary's Integral on HEM Data Inverse Modeling. *Geosciences*, 19 (75), 115- 118.

[31] Everett, M.E., (2013). Near-surface applied geophysics, *Cambridge University Press*.

[32] Zhdanov, M. S. (2015). Inverse theory and applications in geophysics, *Elsevier Science*, 36, 66-97.

[33] Nocedal, J. and Wright, S., (2006). Numerical optimization: series in operations research and financial engineering, *Springer*, New York, USA.

[34] Haber, Eldad (2014). Computational Methods in Geophysical Electromagnetics. Ed. By Thomas A. Grandine Society for Industrial and Applied Mathematics.

[35] Heidari, S. M., Rastad, E., Mohajjel, M., and Shamsa, M. J., (2006). Gold mineralization in ductile shear zone of Kervian (southwest of Saqez-Kordestan province): *Geosciences*, 58, 18–37.

[36] Aliyari, F., Rastad, E., & Zengqian, H. (2007). Orogenic gold mineralization in the Qolqoleh deposit, northwestern Iran. *Resource Geology*, 57(3), 269-282.

[37] Mohajjel, M. & Eshragh, A., (2008). Geological Map of Kervian area, Geological survey of Iran.